J. Fluid Mech. (2020), *vol.* 890, A2. © The Author(s), 2020.
Published by Cambridge University Press
doi:10.1017/jfm.2020.122

Bistability in the unstable flow of polymer solutions through pore constriction arrays

Christopher A. Browne[1], **Audrey Shih**[1] **and Sujit S. Datta**[1,†]

[1]Department of Chemical and Biological Engineering, Princeton University, Princeton, NJ 08544, USA

(Received 6 August 2019; revised 29 December 2019; accepted 9 February 2020)

Polymer solutions are often injected in porous media for applications such as oil recovery and groundwater remediation. As the fluid navigates the tortuous pore space, elastic stresses build up, causing the flow to become unstable at sufficiently large injection rates. However, it is poorly understood how the spatial and temporal characteristics of this unstable flow depend on pore space geometry, which can vary widely between different porous media. We investigate this dependence by systematically varying the spacing between pore constrictions in a one-dimensional ordered array. We find that when the pore spacing is large, unstable eddies form upstream of each constriction, similar to observations of an isolated constriction. By contrast, when the pore spacing is sufficiently small, the flow in the different pores exhibits a surprising bistability, stochastically switching between two distinct unstable flow states. We hypothesize that this unusual behaviour arises from the interplay between elongation and relaxation of polymers as they are advected through the pore space. Consistent with this idea, we find that the flow state in a given pore persists for long times; moreover, flow states are strongly correlated between neighbouring pores. Thus, the characteristics of unstable flow are not determined just by injection conditions and the geometry of the individual pores, but also depend on the spacing between pores. Ultimately, these results help to elucidate the rich array of behaviours that can arise in polymer solution flow through porous media.

Key words: polymers, viscoelasticity, porous media

1. Introduction

Polymer solutions have elastic properties that can dramatically alter their flow behaviour in complex geometries. For example, polymer chains can be elongated as they traverse curved streamlines, generating elastic stresses that modify the flow through the formation of recirculating eddies or flow fluctuations over a range of spatial and temporal scales. Such effects are often harnessed to improve oil recovery and groundwater remediation efforts (Roote 1998; Sorbie 2013; Browne, Shih & Datta 2019). In these cases, an injected polymer solution flows through a tortuous porous medium, such as a reservoir rock or a subsurface aquifer, and displaces trapped non-aqueous fluids from the pore space, enabling them to be recovered downstream.

† Email address for correspondence: ssdatta@princeton.edu

https://doi.org/10.1017/jfm.2020.122 Published online by Cambridge University Press

The spatial and temporal characteristics of the pore-scale flow, which typically depend on the medium geometry (Datta *et al.* 2013; Kang *et al.* 2014; Pak *et al.* 2015; Zami-Pierre *et al.* 2016; Blunt 2017), strongly influence this process: for example, local fluctuations in flow speed may generate local increases in the viscous forces that are thought to help displace trapped fluid (Datta, Dupin & Weitz 2014*a*; Datta, Ramakrishnan & Weitz 2014*b*; Clarke *et al.* 2016; Mitchell *et al.* 2016). It is therefore critical to be able to predict how the flow behaviour depends on the solution properties, injection conditions, and porous medium geometry. Laboratory and field tests provide key empirical measurements of macroscopic variables including fluid pressure and total recovery (Sandiford *et al.* 1964; Durst, Haas & Kaczmar 1981; Pitts *et al.* 1995; Wang, Wang & Xiaem 2011*a*; Vermolen, Van Haasterecht & Masalmeh 2014; Wei, Romero-Zerón & Rodrigue 2014). However, broad application is still limited by an incomplete understanding of how these macroscopic variables depend on the pore-scale features of the fluid flow, which in turn depend on polymer properties, pore space geometry, and imposed flow conditions. As a result, the mechanisms underlying polymer solution-enhanced fluid recovery are still widely debated (Chauveteau & Moan 1981; Chauveteau, Moan & Magueur 1984; Zaitoun *et al.* 1988; Zaitoun, Bertin and Lasseux 1998; Haward & Odell 2003; Odell & Haward 2006; Huh *et al.* 2008; Clarke *et al.* 2016; Mitchell *et al.* 2016; Browne *et al.* 2019), and general principles for predicting and controlling the flow are lacking.

Studies of flow in model microfluidic devices provide valuable insights into the pore-scale flow field. Extensive work has focused on the simplified cases of flow into a single pore constriction or flow into narrow constrictions around a single pillar. In these geometries, the polymer chains are aligned and elongated by the flow, generating upstream recirculating eddies that minimize the extensional stress associated with chain misalignment (Batchelor 1971; Boger 1987; Mongruel & Cloitre 1995, 2003; Rodd *et al.* 2007). Polymer elongation along the curved fluid streamlines also produces normal elastic stresses, which persist for a duration λ before relaxing. Thus, at sufficiently large flow speeds, these stresses build up in the solution, further perturbing the flow and causing an elastic instability to arise: an unsteady flow state develops in which the eddies have a broad spectrum of spatial and temporal fluctuations (Koelling & Prud'homme 1991; Lanzaro & Yuan 2011; Kenney *et al.* 2013; Ribeiro *et al.* 2014; Gulati, Muller & Liepmann 2015; Lanzaro, Li & Yuan 2015; Shi *et al.* 2015; Shi & Christopher 2016; Lanzaro, Corbett & Yuan 2017; Haward, Toda-Peters & Shen 2018; Qin *et al.* 2019). A similar instability also arises in other flows with highly curved fluid streamlines (Pearson 1976; Larson 1992; McKinley, Pakdel & Öztekin 1996; Pakdel & McKinley 1996; Groisman & Steinberg 2000; Pan *et al.* 2013; Galindo-Rosales *et al.* 2014; Sousa *et al.* 2015; Haward, McKinley & Shen 2016; Qin & Arratia 2017). However, it is unclear how these effects manifest in a porous medium composed of many successive pore constrictions and expansions, known as throats and bodies, respectively.

Imaging of flow through one-dimensional (1-D) arrays of widely spaced pore throats consistently demonstrates the formation of unstable eddies upstream of each throat, similar to the case of an isolated throat (Khomami & Moreno 1997; Arora, Sureshkumar & Khomami 2002; Galindo-Rosales *et al.* 2012; Kenney *et al.* 2013; Shi *et al.* 2015; Varshney & Steinberg 2017). By contrast, when the spacing between pore throats is small, chain elongation may persist across multiple pores as the polymers are advected through the pore space. Thus, memory of strain in one pore may influence the flow in a pore further downstream, potentially imparting new

https://doi.org/10.1017/jfm.2020.122 Published online by Cambridge University Press

spatio-temporal structure to the flow. However, this possibility remains to be explored. Studies conducted at a Reynolds number $Re \sim 20$ and an elasticity number $El \sim 1$, and thus also subject to inertial effects, show that decreasing the spacing between pores produces stronger flow fluctuations (Shi & Christopher 2016) – providing a clue that polymer memory may indeed influence the flow. Nevertheless, whether and how polymer memory impacts flow through a porous medium has not been fully resolved for the case of $Re \ll 1$ and $El \gg 1$, in which elastic effects dominate and inertial effects do not also arise. This flow regime is particularly relevant to key applications including oil recovery and groundwater remediation, which can have Re ranging from $\sim 10^{-11}$ to 10^{-3} and El ranging from $\sim 10^{2}$ to 10^{11}.

Here, we use confocal microscopy to investigate the unstable flow of an elastic polymer solution through a 1-D ordered array of pores at $Re \ll 1$ and $El \gg 1$. This model geometry provides a way to systematically vary the spacing between pores, enabling us to isolate and directly test the relative importance of polymer memory on the flow behaviour. When the spacing between pores is large, unstable eddies form upstream of each throat, similar to observations of an isolated throat. By contrast, when the spacing between pores is sufficiently small, the flow exhibits a surprising bistability. In each pore body, the flow persists over long durations in one of two distinct flow states: an eddy-dominated state in which a pair of large unstable eddies forms in the corners of the pore body, and an eddy-free state in which strongly fluctuating fluid pathlines fill the entire pore body and eddies do not form. We hypothesize that this unusual behaviour arises from the interplay between flow-induced polymer elongation, which promotes eddy formation, and relaxation of polymers as they are advected between pores, which enables the eddy-free state to form. Consistent with this idea, we find that the flow state in a given pore persists for long times. In addition, we find that the instantaneous flow state is correlated between neighbouring pores; however, these correlations do not persist over long times. Thus, our results reveal that the characteristics of unstable flow are not determined just by injection conditions and the geometry of the individual pores, but also depend on the spacing between pores. Ultimately, these results help to elucidate the rich array of behaviours that can arise in polymer solution flow through porous media.

2. Materials and methods

The void space of a porous medium is typically composed of successive expansions known as pore bodies connected by narrower constrictions known as pore throats (Doyen 1988; Kwiecien, Macdonald & Dullien 1990; Bernabe 1991; Ioannidis & Chatzis 1993). We use three-dimensional (3-D) printing to make model porous media that recapitulate these geometric features (O'Connell *et al.* 2019). Importantly, this approach provides precise control over the pore space geometry, and yields devices that can be optically interrogated while also withstanding the high pressures that arise during elastic polymer solution flow.

The media are made of straight, square channels having constrictions defined by evenly spaced hemi-cylindrical posts, as illustrated in figure 1. For simplicity, this geometry thus does not incorporate complex pore space tortuosity and connectivity; instead, it provides a way to isolate and systematically probe the role of pore spacing on flow behaviour. Each channel is $W = 2$ mm wide, $H = 2$ mm high and 7 cm long, with opposing posts of diameter $D_p = 1.6$ mm that are laterally separated by $L_c = 0.4$ mm and spaced by a centre-to-centre distance of l_s along the flow direction. The space between hemi-cylinders along the flow direction thus defines the pore bodies,

https://doi.org/10.1017/jfm.2020.122 Published online by Cambridge University Press

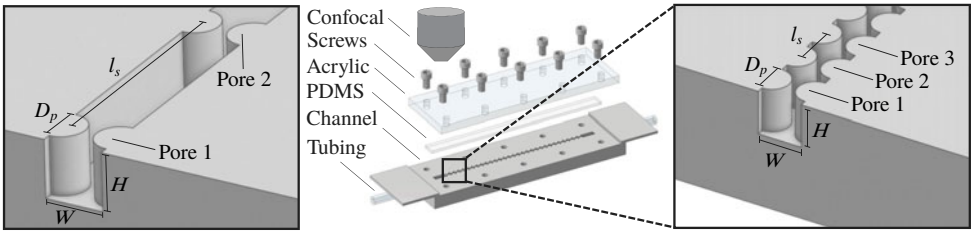


FIGURE 1. Experimental set-up. Fluidic channel contains pore throat constrictions defined by opposing hemi-cylindrical posts and is fabricated using a stereolithographic 3-D printer. Dimensions are $W = 2$ mm, $H = 2$ mm, $D_p = 1.6$ mm. We vary the pore throat separation distance l_s and the number of throats in the channel (two examples are shown in the left and right panels). The channel is screwed shut with an acrylic plate over a thin strip of PDMS. Inlet and outlet tubing is glued into 3-D printed holes. The set-up is inverted and videos are captured on a confocal microscope; the middle panel is vertically flipped for clarity.

while the lateral constriction between opposing hemi-cylinders defines the pore throats. Varying l_s provides a way to systematically test the influence of pore spacing on the flow; hence, our experiments probe an isolated pore throat with $l_s \to \infty$, a pair of throats with $l_s = 16W$, and an array of 30 throats with $l_s = 1W$.

To fabricate each device, we 3-D print the open-faced channel with a FormLabs Form 2 stereolithography printer, using a proprietary clear polymeric resin (FLGPCL04) composed of methacrylate oligomers and photoinitiators. We then glue inlet and outlet tubing directly into 3-D printed connectors designed to minimize perturbation of the polymers away from the pores. Finally, as shown in figure 1, the whole assembly is screwed shut using a clear acrylic sheet laser cut to size and placed on top of a thin strip of polydimethylsiloxane (PDMS), which provides a watertight seal.

The fluid used is an aqueous solution of 18 MDa partially hydrolyzed polyacrylamide (HPAM, 30 % carboxylated monomers; Polysciences), a polymer commonly used in oil recovery (Sandiford *et al.* 1964; Wei *et al.* 2014). We dissolve 300 ppm HPAM in a solvent of 10 vol% ultrapure water (Millipore) and 90 vol% glycerol (Sigma Aldrich) containing 1 wt% NaCl (Sigma Aldrich). We use dynamic light scattering to directly measure the mean polymer radius of gyration R_g for a dilute solution of 30 ppm HPAM in the same solvent mixture used in the flow experiments. We find $R_g \approx 196$ nm; furthermore, we estimate the polymer overlap concentration via the relation $C^* \approx (M_w/V)/N_A$, where M_w is the polymer molecular weight, $V = 4\pi R_g^3/3$ is the volume occupied by a single polymer molecule, and N_A is Avogadro's number (Rubinstein & Colby 2003). This calculation yields an overlap concentration of $C^* \approx 940$ ppm and therefore our experiments use a dilute polymer solution at ≈ 0.3 the overlap concentration. We also seed the polymer solution with 1 ppm of fluorescent 1 μm polystyrene tracer particles (Invitrogen) to enable flow visualization; the particles have excitation between 480 and 510 nm with an excitation peak at 505 nm, and emission between 505 and 540 nm with an emission peak at 515 nm. For each medium geometry tested, we prepare a fresh solution and use it within one month.

The channel dimensions and polymer concentration used in our experiments enable us to isolate the influence of polymer elongation and relaxation between pores, with

https://doi.org/10.1017/jfm.2020.122 Published online by Cambridge University Press

a minimal influence of polymer surface adsorption, flow-induced chain migration, wall slip, shear banding and polymer entanglement. As described further in the Appendix, we expect that polymer adsorption, migration and wall slip occur over length scales ~ 0.1 to 10 μm, over one to three orders of magnitude smaller than the smallest channel dimension $L_c = 400$ μm. Also, as described further in the Appendix, we expect that shear banding and polymer entanglement effects do not occur for the dilute concentrations explore here. However, such effects could play a role in the flow of more concentrated polymer solutions in media with smaller pores.

To visualize the flow, we invert and mount each assembled device on a Nikon A1R inverted laser-scanning confocal microscope. The polymer solution is subsequently injected through the porous medium at a fixed volumetric flow rate Q using a syringe pump (Harvard Apparatus PHD 2000). The time required to inject a single pore throat volume is then given by $\tau_{pv} \equiv V_{pv}/Q$, where we define the pore throat volume as the void volume between the beginning and end of a pair of opposing hemi-cylinders, $V_{pv} = D_p WH - \pi D_p^2 H/4$. In our experiments at sufficiently large Q, we find that unstable fluctuations begin after $\approx 10\tau_{pv}$ and continue to develop over a time scale of $\approx 40\tau_{pv}$, after which it reaches a dynamic equilibrium in which the statistical properties of the flow, described in § 3, do not appreciably change. Our flow visualization measurements are thus taken $\approx 300\tau_{pv}$ after initiating the flow to ensure that the unstable state is fully developed. For imaging, we use a green laser with an excitation wavelength of 488 nm and detection in the range 500–550 nm, which enables us to identify the individual fluorescent particles. We employ resonant scanning, in which the laser is raster scanned over each pixel sequentially, with a CFI60 Plan Apochromat Lambda 4X objective lens with 0.2 numerical aperture. This set-up enables us to continually raster a field of view of 2127 μm by 2127 μm. We acquire fluorescence images every 33 ms, or at 30 frames per second, from an optical slice of 17.9 μm thickness in the centre of the channel height. To visualize the pathlines of the individual tracer particles, we average successive frames for $10\tau_{pv}$, yielding the micrographs shown hereafter.

We characterize the solution rheology using an Anton Paar MCR-501 rheometer with a 50 mm 1° cone-plate geometry. Figure 2 shows the measured shear stress σ and first normal stress difference N_1 over different shear rates $\dot{\gamma}$ for a representative solution. Furthermore, to assess possible degradation of polymers due to unstable flow in the porous media (Vanapalli, Ceccio & Solomon 2006), we also measure the solution rheology after performing flow experiments at the highest flow rates tested. We find no significant difference between the solution rheology measured before (dark blue points in figure 2) and after (light blue points) flow experiments, indicating minimal polymer degradation due to the unstable flow. For each solution used in each experiment, we obtain at least five replicate measurements of the fluid rheology and use the averaged values in all subsequent calculations.

The shear stress varies approximately linearly with shear rate, with a shear thinning exponent ≈ 0.92, indicating that shear thinning effects are small due to the high viscosity of the background solvent. Indeed, the pure solvent viscosity is approximately 0.6 times the measured solution viscosity. However, for accuracy, we use the rate-dependent shear viscosity $\mu(\dot{\gamma}) \equiv \sigma(\dot{\gamma})/\dot{\gamma}$ in all calculations. The shear rate varies widely within the complex geometry used in our experiments; therefore, to determine a shear rate that characterizes each experiment, we evaluate the wall shear rate in the pore throat at each value of Q tested, since it is the maximal shear rate in our system. We do this using the flow profile for a non-Newtonian fluid having the measured shear-thinning exponent 0.92, as calculated by Harnett & Irvine (1979) and

https://doi.org/10.1017/jfm.2020.122 Published online by Cambridge University Press

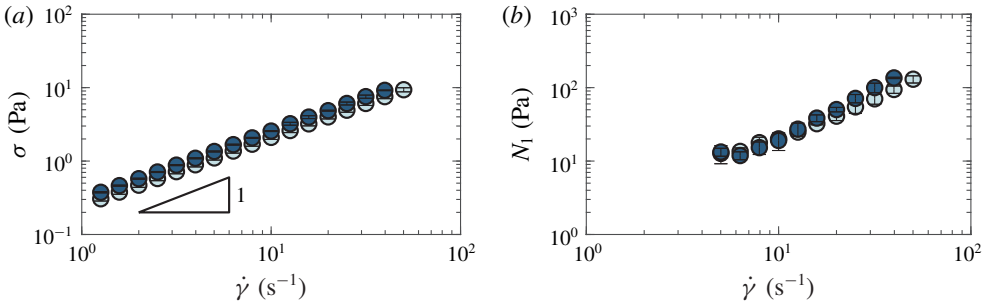


FIGURE 2. Rheology of HPAM polymer solutions. Panel (*a*) shows the shear stress σ and panel (*b*) shows the first normal stress difference N_1 as functions of the shear rate $\dot{\gamma}$ for the sample used for figures 4(*c*), 6, 7 and 8(*b–d*). Data are taken before (dark blue) and after (light blue) a porous media flow experiment, showing that polymers are not appreciably degraded by the unstable flow. Error bars represent standard deviation over five replicate rheological measurements. Fresh polymer solutions are prepared for each experiment, and all dimensionless quantities described in the text are calculated using rheology on fresh samples.

by Son (2007). We use this choice of the maximal shear rate to estimate characteristic values of the fluid Reynolds number, Weissenberg number, elasticity number and the M parameter, as described further below. In particular, this choice of wall shear rate enables us to provide upper bounds for the fluid Reynolds numbers $\ll 1$, ensuring that inertia is negligible throughout the flow, as well as the M parameter, whose maximal value is believed to generate unstable flow (Grilli, Vázquez-Quesada & Ellero 2013).

We define the Reynolds number comparing inertial to viscous stresses as $Re \equiv \rho U_t L/\mu(\dot{\gamma})$, where ρ is the density of the solvent, $U_t \equiv Q/A_t$ is the speed corresponding to flow through the pore throat cross-section $A_t = (W - D_p)H$, and the length scale L is chosen to be half the constriction width, $\frac{1}{2}(W - D_p)$. This estimate represents an upper bound for the Reynolds number characterizing the flow; in our porous media experiments, Re ranges from $\approx 8 \times 10^{-5}$ to 7×10^{-3}, indicating that viscous stresses dominate over inertial stresses.

Another common descriptor of elastic flows is the Weissenberg number, which compares elastic stresses to viscous stresses. We define this parameter as $Wi \equiv N_1(\dot{\gamma})/2\sigma(\dot{\gamma})$, following convention. In our porous media experiments, Wi ranges from ≈ 2 to 9, indicating that elastic stresses dominate. Moreover, the corresponding values of the elasticity number $El \equiv Wi/Re$, which compares elastic stresses to inertial stresses, are $\gtrsim 900$. Our experiments thus probe the elasticity-dominated flow regime.

An elastic instability arises when elastic stresses – characterized by a large value of Wi – persist over curved streamlines. This persistence of elastic stresses occurs if the flow time scale $U_t/\mathscr{R}$, where $\mathscr{R}$ is the streamline radius of curvature, exceeds the polymer relaxation time λ. Thus, elastic stresses build up in the flow, leading to the generation of unstable flow, when the parameter $M \equiv \sqrt{2Wi \cdot \lambda U_t/\mathscr{R}}$ exceeds a threshold value, as confirmed experimentally for diverse flow geometries (McKinley *et al.* 1996; Pakdel & McKinley 1996; Zilz *et al.* 2012; Haward *et al.* 2016). Indeed, the M parameter is derived from a linear stability analysis of the Stokes equation for a viscoelastic fluid (McKinley *et al.* 1996; Pakdel & McKinley 1996); specifically, it represents the order of the largest destabilizing term in the Stokes equation, which leads to the generation of unsteady flow. Therefore, M parameterizes the onset of flow

https://doi.org/10.1017/jfm.2020.122 Published online by Cambridge University Press

instability due to fluid elasticity, and we use this parameter to describe the different flow regimes tested in our experiments. We evaluate M using the wall shear rate in the pore throat at each value of Q tested, since this produces the maximal shear rate and therefore the highest local M, which is believed to generate unstable flow (Grilli *et al.* 2013). For this value of the shear rate, we then use our measurements of polymer solution rheology to calculate Wi as well as the rheological relaxation time $\lambda = Wi/\dot{\gamma}$. We find $\lambda \approx 0.3$ to 6 s, in good agreement with previous measurements performed on similar solutions (Qin & Arratia 2017). Additionally, we calculate the streamline radius of curvature using the empirical expression determined by McKinley *et al.* (1996) for the onset of unstable flow around a cylindrical post of diameter D_p centred within a channel of width W: $\mathscr{R} \approx (2/D_p + 32.5/W)^{-1}$, where D_p and W are as illustrated in figure 1. We note that in our experiments, the posts are wall-centred instead of channel-centred; determining whether and how this difference in geometry influences $\mathscr{R}$ will be a useful direction for future theoretical work. Using the calculated values of Wi, λ and $\mathscr{R}$, we then calculate $M \equiv \sqrt{2Wi \cdot \lambda U_t/\mathscr{R}}$. The corresponding values of M range from ≈ 6 to 31 for our experiments.

3. Results

3.1. *Isolated pore throat*

To test the limiting case of widely spaced pores ($l_s \to \infty$), we first investigate flow through an isolated pore throat centred in a channel. At low imposed flow rates, and thus at low values of M, the flow is laminar: the fluid pathlines do not cross and do not change in time. We do not observe eddies – instead, the pathlines smoothly converge as they approach the throat and symmetrically diverge as they leave it. However, above a threshold value of $M \approx 19$, we observe the onset of a flow instability: a pair of unstable eddies forms against the channel walls upstream of the pore throat, as exemplified in figures 3(*a–c*) (at the pore throat) and 3(*d–f*) (upstream) for $M = 19.4$, 23.9 and 30.5.

Within each eddy, the fluid recirculates with a speed slower than the mean imposed flow speed in the channel. The fluid pathlines continually fluctuate on long time scales, and also continually cross, indicating that fluctuations in the flow occur on a time scale shorter than the pathline duration of $10\tau_{pv}$ (figure 3*d–f*). These fluctuations are reflected in the motions of the eddy boundaries and lengths, which also fluctuate as the flow progresses. Similarly, while the fluid in the region formed between the eddies does not recirculate, the fluid pathlines also continually fluctuate on long time scales and continually cross, reflecting the presence of rapid fluctuations in the flow throughout. By contrast, the flow is more steady downstream of the pore throat: we do not observe any eddies or marked temporal changes in the flow for all values of M tested. This result is consistent with the findings of Qin *et al.* (2019), who also found highly unstable eddies upstream of a cylinder in a channel, but suppressed fluctuations and no eddies downstream. We therefore focus our subsequent analysis on the upstream region.

To further characterize this behaviour, we track the eddy length L_{eddy} over time for each value of M tested. We measure L_{eddy} from the base of the hemi-cylinders ($x = 0$ in figure 3*d*) to the farthest upstream location having a pathline oriented perpendicular to the imposed flow direction (dashed lines in figure 3*d–f*). Consistent with the visual observations, L_{eddy} fluctuates over time in each experiment, as indicated by the shaded regions in figure 3(*g–i*); however, it fluctuates around a single mean value that increases with M. We quantify these fluctuations using the coefficient of

https://doi.org/10.1017/jfm.2020.122 Published online by Cambridge University Press

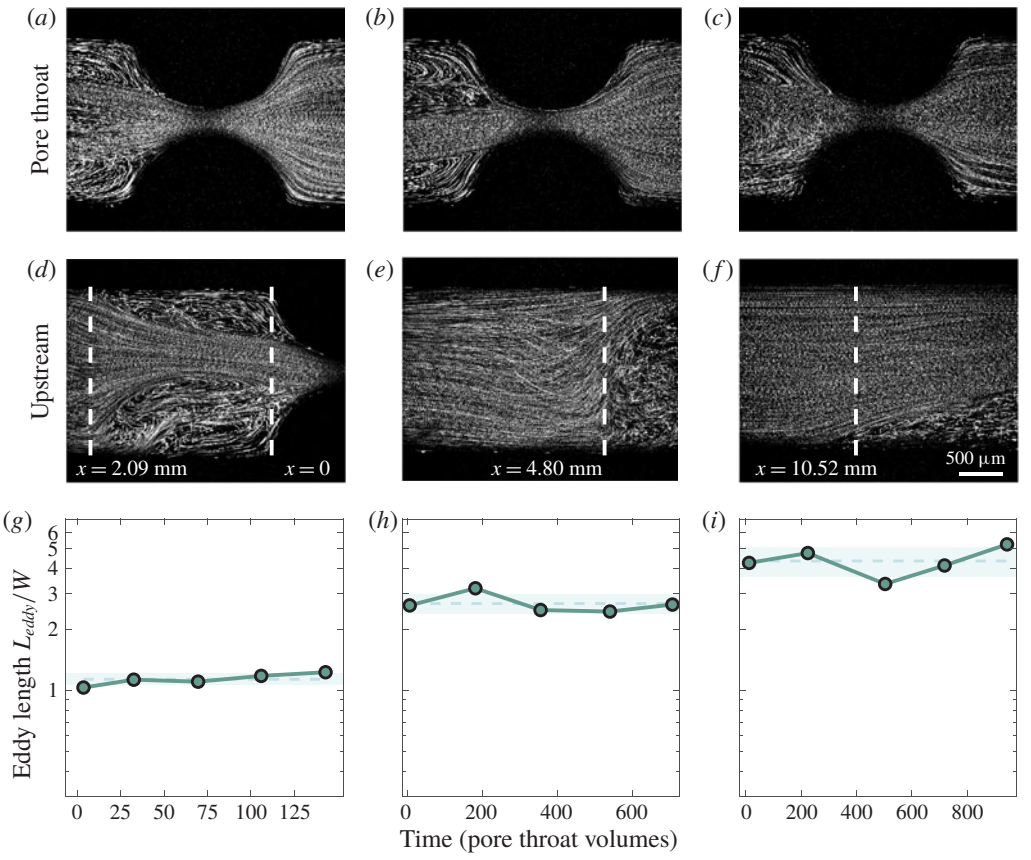


FIGURE 3. Pathline images of polymer solution flow through a straight channel with a single pore throat. Pathline images are averaged over $10\tau_{pv}$. Flow rates are expressed via the M parameter, which equals 19.4, 23.9 and 30.5 for panels (*a*), (*b*) and (*c*), respectively, corresponding to Weissenberg numbers $Wi = 5.6$, 6.9 and 8.8. Panels (*a–c*) show strong recirculating eddies upstream of the pore throat, but no downstream eddies at any flow rate. Panels (*d–f*) show the leftmost edge of the eddies in front of the pore throat. Dashed lines indicate where the eddy-dominated region begins. Here, x indicates the distance in millimetres from the base of the hemi-cylinder. Panels (*g–i*) show the measured eddy length over time normalized by τ_{pv}. Shaded regions show standard deviation around the temporal mean (dashed lines).

variation c_v, defined as the ratio between the standard deviation and the mean of the measurements of L_{eddy} over time. Taking data from two replicate experiments at these imposed flow rates, we find $c_v \approx 0.3$, 0.3 and 0.4 for $M = 19.4$, 23.9 and 30.5, respectively.

We summarize all of our measurements by plotting the probability density (p.d.f.) of time-averaged measured eddy lengths for each value of M tested. Below the threshold value of $M \approx 19$, we do not observe eddies and hence $L_{eddy} = 0$. By contrast, above this threshold, $L_{eddy} > 0$ fluctuates about a well-defined mean value, which increases with M, as shown in figure 4(*a*). This increase in L_{eddy} is similar to previous measurements for isolated constrictions; these studies demonstrate that eddies form when polymers

https://doi.org/10.1017/jfm.2020.122 Published online by Cambridge University Press

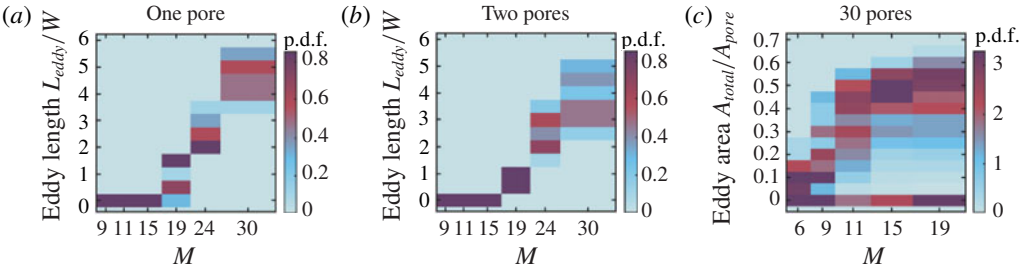


FIGURE 4. Probability density functions of measured eddy sizes for different values of M, averaged over at least $7\tau_{pv}$ and over two separate replicate experiments, displayed vertically as heatmaps. (*a*) Probability density functions of L_{eddy}/W for a channel with a single pore throat constriction. For each value of M there is a single characteristic eddy length that increases monotonically with M. (*b*) Probability density functions of L_{eddy}/W for a channel with two widely spaced pores $l_s = 16W$ apart. Again, for each value of M there is a single characteristic eddy length that increases monotonically with M. (*c*) Probability density functions of A_{total}/A_{pore} for a porous medium with 30 closely spaced pores $l_s = W$ apart. Here, the probability density functions for $M > 9$ are bimodal, showing multiple characteristic eddy areas (one peak at $A_{eddy}/A_{pore} \approx 60\,\%$ and one peak at $A_{eddy}/A_{pore} \approx 0$). The two branches in the probability density functions indicate a bistability in unstable flow states.

are elongated, and the size of eddies grows as polymers are increasingly elongated (Batchelor 1971; Boger 1987; Mongruel & Cloitre 1995, 2003; Rodd *et al.* 2007). Our results thus suggest that flow fluctuations arising from unstable flow elongate the individual polymer chains (Sureshkumar, Beris & Handler 1997; Balkovsky, Fouxon & Lebedev 2000; Chertkov 2000; Gupta, Sureshkumar & Khomami 2004; Terrapon *et al.* 2004), which then generate unstable upstream eddies to minimize extensional stresses (Batchelor 1971; Boger 1987; Mongruel & Cloitre 1995, 2003; Rodd *et al.* 2007).

3.2. *Two widely spaced pore throats*

We next investigate two pore throats spaced a distance $l_s = 16W$ apart along the flow direction. As we find with an isolated throat, the flow is laminar at low values of M, while above a similar threshold value of $M \approx 19$, we observe the onset of the flow instability. A pair of unstable eddies again forms against the channel walls upstream of each pore throat, as exemplified in figures 5(*a–c*) (first throat) and 5(*d–f*) (second throat). Moreover, as with the isolated pore throat, the flow is more steady immediately downstream of each throat, with no observable eddies or temporal changes in the flow for any values of M tested.

We again quantify this behaviour by measuring L_{eddy} over time for each value of M tested. For each pore throat, L_{eddy} again fluctuates around a single mean value that increases with M (figure 5*g–i*) – similar to the case of an isolated throat. The p.d.f.s of the combined time-averaged measurements of L_{eddy} also reflect its increase with M, as shown in figure 4(*b*). Intriguingly, however, we observe two key differences from the isolated throat. First, while the mean values of L_{eddy} are similar for the two pore throats, eddies upstream of the second throat (red points, figure 5*g–i*) are

https://doi.org/10.1017/jfm.2020.122 Published online by Cambridge University Press

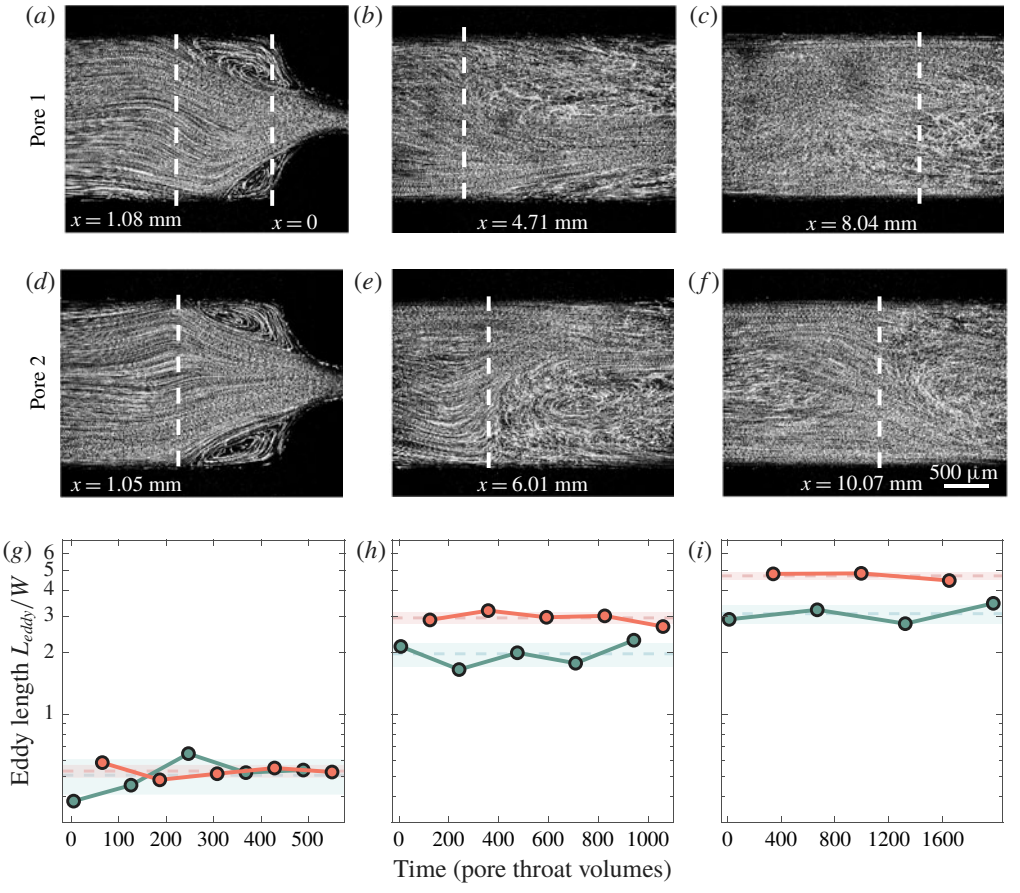


FIGURE 5. Pathline images of polymer solution flow through a straight channel with two pore throats separated by $l_s = 16W$. Pathline images are averaged over $10\tau_{pv}$. Flow rates are expressed via the M parameter, which equals 19.4, 23.9 and 30.5 for (*a*), (*b*) and (*c*), respectively, corresponding to $Wi = 5.6$, 6.9 and 8.8. Panels (*a–c*) show the leftmost edge of the eddies in front of the first pore throat. Panels (*d–f*) show the leftmost edge of the eddies in front of the second pore throat. No eddies are observed downstream of either throat. Panels (*g–i*) show the measured eddy lengths over time normalized by τ_{pv} for pore 1 (green) and pore 2 (red). Shaded regions show standard deviation around the temporal mean (dashed lines).

slightly larger than eddies upstream of the first throat (green points) for large values of M. Second, the eddies upstream of the second throat are less unstable – the temporal fluctuations in L_{eddy} are notably suppressed for the second pore throat for all M above the threshold for unstable flow (compare red to green shaded regions in figure 5*g–i*). Comparing the coefficients of variation confirms this finding: for the first pair of eddies, $c_v = 0.2 \pm 0.1$ while for the second pair, $c_v = 0.10 \pm 0.02$, which is significantly smaller ($p = 0.02$, one-tailed t-test). Thus, when the spacing between pore throats is reduced, the spatio-temporal characteristics of the flow are altered – presumably because polymer elongation can persist across multiple pores.

https://doi.org/10.1017/jfm.2020.122 Published online by Cambridge University Press

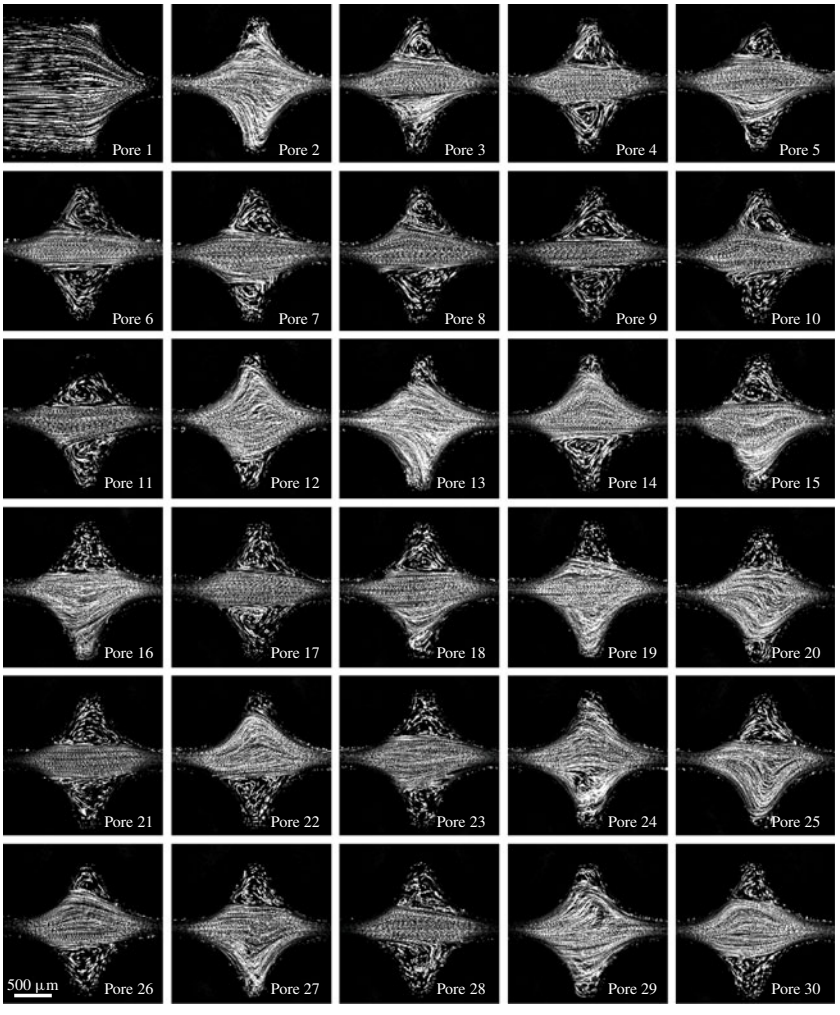


FIGURE 6. Pathline images of polymer solution flow through a porous medium with 30 pore throats separated by $l_s = W = 2$ mm at $M = 11.4$. Images span 2.11 mm across. Pathline images are averaged over $10\tau_{pv}$. Pore 6 exemplifies the eddy-dominated state, with eddies that continually fluctuate both internally and at their boundaries, while pore 2 exemplifies the eddy-free state, with strongly fluctuating pathlines that fill the entire pore body.

3.3. *Thirty closely spaced pore throats*

To further test the hypothesis that polymer memory impacts flow behaviour, we next investigate flow through a medium with an even smaller spacing between pore throats. Specifically, the flow channel contains 30 pore throats spaced a distance $l_s = W$ apart along the flow direction. In this case, we find that the flow behaviour is strikingly different from the larger l_s cases described in §§ 3.1 and 3.2.

One key difference is that the threshold for the onset of the flow instability is dramatically lowered. At low imposed flow rates, and thus at low values of M, the

https://doi.org/10.1017/jfm.2020.122 Published online by Cambridge University Press

flow is laminar: the fluid pathlines do not cross and do not vary over time. In this regime, a pair of small, symmetric, laminar, recirculating eddies forms in the corners of each pore body due to the small spacing between successive pore expansions and constrictions. Above a threshold value of $M \approx 9$ – considerably smaller than the threshold $M \approx 19$ for the single- and double-throat cases – we observe the onset of unstable flow: the fluid pathlines continually cross and vary over time. Thus, decreasing the spacing between pore throats decreases the threshold value of M required for unstable flow, suggesting that polymer memory strongly impacts the flow behaviour.

Even more strikingly, we observe two distinct flow states that can arise in each pore body throughout the medium: an 'eddy-dominated' state in which a pair of large unstable eddies forms in the corners of the pore body, and an 'eddy-free' state in which strongly fluctuating fluid pathlines fill the entire pore body and eddies do not form. This surprising bistability is illustrated in figure 6, which shows the pathline images taken sequentially from each pore in the medium at $M = 11.4$. Pore 6 exemplifies the eddy-dominated state, with eddies that continually fluctuate both internally and at their boundaries, while pore 2 exemplifies the eddy-free state, with strongly fluctuating pathlines that fill the entire pore body. Though these snapshots are taken at an optical slice in the centre of the channel height, imaging at other heights shows similar flow pathlines, indicating that the spatial structure of the flow does not vary appreciably across the channel height. This observation is in stark contrast to the typical assumption that flow behaviour in a porous medium is determined just by injection conditions and the geometry of the individual pores (Zami-Pierre *et al.* 2016). Instead, we find that different pores can exhibit distinct flow characteristics, even when the individual pore geometries and imposed flow rates are all identical.

To quantify this behaviour, we measure the two-dimensional (2-D) area of the individual eddies A_{eddy} over time for each value of M tested. In laminar flow, the eddies occupy only $\approx 5\,\%$ of the total area of a pore, which we define as $A_{pore} \equiv Wl_s - \pi D_p^2/4$. By contrast, unstable eddies in the eddy-dominated state have values of A_{eddy} that fluctuate strongly in time, and whose mean value can be up to $\approx 30\,\%$ of A_{pore}, while in the eddy-free state $A_{eddy} \approx 0$. Intriguingly, while the two flow states are each unstable, the flow behaviour in each pore body appears to be bistable, as illustrated in figure 7: a pore will persist in a given unstable flow state for a long duration of time before switching, seemingly randomly, to the other flow state. For example, at $M = 11.4$, the upper eddy in pore 13 and the lower eddy in pore 14 (figure 7*g*, upward-pointing red triangles and downward-pointing green triangles, respectively) persist in the eddy-dominated state over the entire imaging duration, while the lower eddy in pore 13 persists in the eddy-free state (downward red triangles). However, the upper eddy in pore 14 initially switches from the eddy-free to the eddy-dominated state, in which it persists for $15\tau_{pv}$ before switching back to the eddy-free state (upward green triangles). We observe this flow bistability in all pores of the medium, and at all values of M tested; two more examples for $M = 15$ and 19.4 are shown in figure 7(*h–i*), respectively.

To further characterize the flow bistability shown in figure 7(*g–i*), we plot the p.d.f.s of the time-averaged measurements of A_{total}, which describes the total A_{eddy} measured in each pore combined for all 30 pores in the medium. Below $M \approx 9$, $A_{total} \approx 10\,\%$ of A_{pore}, and eddies do not change in time; by contrast, above the onset of the flow instability at $M \approx 9$, the p.d.f.s become bimodal, reflecting the bistability in flow behaviour (figure 4*c*). The eddy-dominated state is represented by the upper

https://doi.org/10.1017/jfm.2020.122 Published online by Cambridge University Press

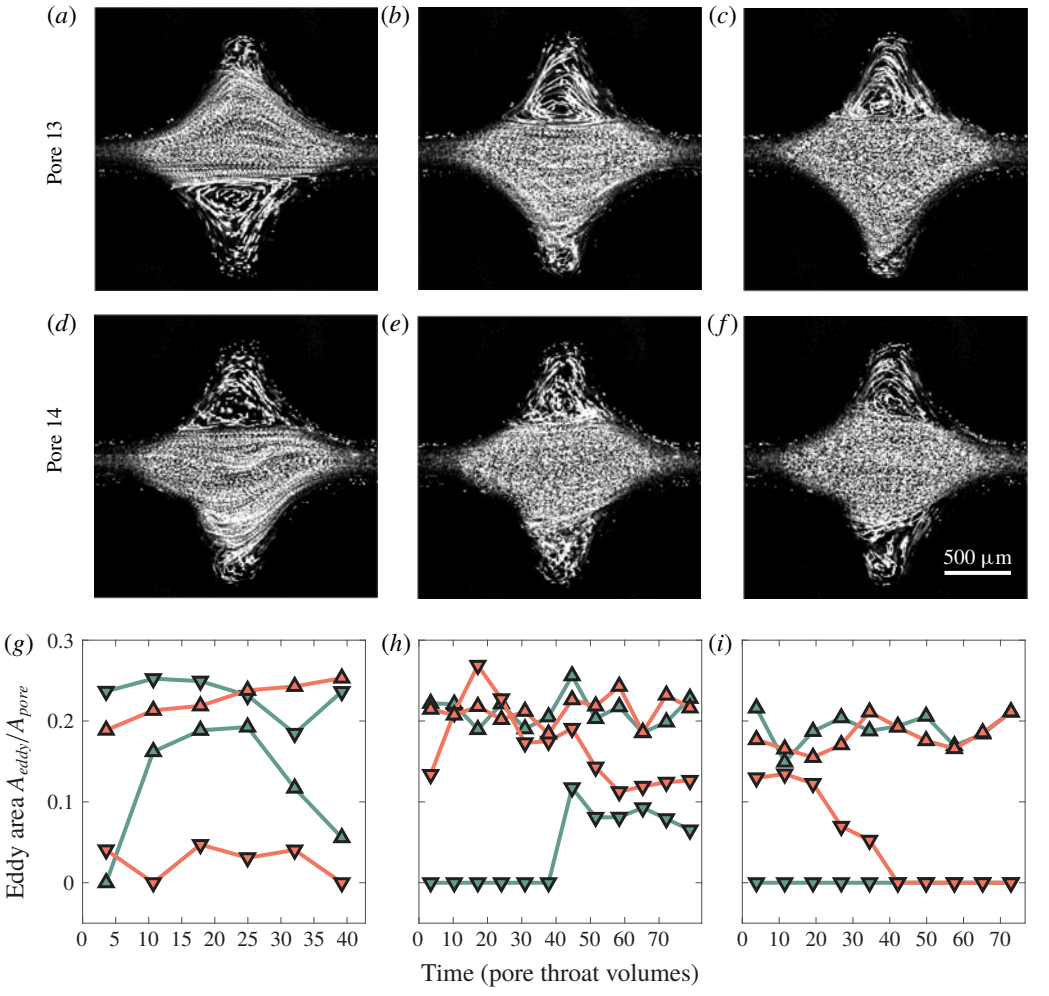


FIGURE 7. Pathline images of polymer solution flow through pores 13 (*a–c*) and 14 (*d–f*) at different flow rates corresponding to $M = 11.4$, 15 and 19.4 (left to right). Pathline images are averaged over $10\tau_{pv}$. Panels (*g–i*) show the measured eddy areas A_{eddy}/A_{pore} over time normalized by τ_{pv} for pore 13 (green) and pore 14 (red). Upward triangles are for the top region of the pore body, downward triangles are for the bottom region of the pore body.

branch of the p.d.f.s, in which A_{total} increases with M, eventually plateauing at $\approx 60\,\%$ of A_{pore} at the highest values of M tested. The eddy-free state is represented by the lower branch of the p.d.f.s, in which $A_{total} \approx 0$ over all M. This bistability does not arise in porous media with wider pore spacings: the lower branch of the p.d.f.s does not appear in figure 4(*a*,*b*). Thus, when the spacing between pore throats is reduced from $l_s = 16W$ to $l_s = W$ – and thus, elongation of individual polymers is more likely to persist across multiple pores – the flow abruptly becomes bistable, exhibiting two coexisting unstable flow states. Indeed, previous work has theorized that unstable flow

https://doi.org/10.1017/jfm.2020.122 Published online by Cambridge University Press

may bifurcate into two coexisting flow states (Avgousti & Beris 1993; Sureshkumar, Beris & Avgousti 1994; Varshney & Steinberg 2017); to our knowledge, our work is the first experimental confirmation of this prediction.

3.3.1. *Bistability and polymer conformations in flow*

How does this unusual flow bistability arise? Previous measurements of polymer conformations indicate that differing fractions of coiled and elongated chains coexist in extensional and unstable flows depending on the imposed flow conditions (Schroeder *et al.* 2003; Gerashchenko, Chevallard & Steinberg 2005; François *et al.* 2009). Furthermore, simulations indicate that polymers having different elongation can have dramatically differing pore-scale flow behaviours (Pilitsis & Beris 1989, 1991). Thus, we hypothesize that flow bistability arises from the interplay between flow-induced polymer elongation, which promotes eddy formation, and relaxation of polymers as they are advected between pores, which enables the eddy-free state to form.

We first consider a pore in the eddy-dominated state. Polymers entering the pore are likely in an elongated conformation due to the combined influence of unstable flow fluctuations and extension by flow converging into the upstream pore throat. Indeed, previous work has demonstrated that eddies form upstream of a constriction when polymers are elongated (Batchelor 1971; Boger 1987; Mongruel & Cloitre 1995, 2003; Rodd *et al.* 2007). Eddy formation minimizes extensional stresses in the centre of the pore: the net flow through the pore body occurs in a nearly straight channel spanning one pore throat to the next, as can be seen in the example of pore 6 in figure 6. For simplicity, we consider the limit of large M, in which eddies completely fill the corners of the pore body. With the exception of unstable fluctuations, the flow velocities in this channel are then aligned along the flow direction with speed $\sim U_t \equiv Q/A_t \sim 1$ mm s^{-1}, and therefore the extensional component of the flow in the channel is minimal. The elongated polymers thus continue to relax as they are advected through this channel, reaching their equilibrium coiled conformation after a duration $\sim \lambda_{rel}$, the chain relaxation time. We compare this time scale to the residence time required for the polymers to transit across the pore body from the upstream throat to the downstream throat, $\sim l_s/U_t$, yielding an advective Deborah number $De_{adv} \equiv \lambda_{rel} U_t/l_s$. When l_s is small and $De_{adv} \gtrsim 1$, chains are still elongated as they enter the next pore body, thereby promoting eddy formation in the current pore and the downstream pore as well. For our experiments in the unstable regime with $l_s = W$, De_{adv} ranges from ~ 0.5 to 3 using $\lambda_{rel} \sim \lambda \approx 1$ s; this estimate likely underestimates De_{adv}, since λ_{rel} is known to increase considerably in extensional flow (Clasen *et al.* 2006). Thus, we expect the eddy-dominated state to persist in the pore body over time before random flow fluctuations cause it to switch to the eddy-free state, consistent with our measurements shown in figure 7(*g–i*). We also expect the eddy-dominated state to be correlated between neighbouring pores.

We next consider the formation of the eddy-free state. As polymers pass through eddy-dominated pores, they gradually relax to the coiled conformation. When a sufficient fraction of coiled polymers are at the entrance to a pore, there will be no driving force for eddy formation. The pore will thus be in the eddy-free state. The fluid streamlines then diverge from the upstream pore throat, creating a compressional flow that further promotes the coiled conformation. As the polymers continue to traverse the pore body, they remain coiled until they encounter the converging flow into the downstream pore throat. This extensional flow partially elongates the chains, which requires a time scale $\sim \lambda_{ret}$. We again compare this time scale to the residence

https://doi.org/10.1017/jfm.2020.122 Published online by Cambridge University Press

time required for the polymers to transit from the beginning of the converging region to the downstream throat, in this case $\sim H(WD_p/2 - \pi D_p^2/8)/Q$. This comparison yields another advective Deborah number $De'_{adv} \equiv \lambda_{ret} Q/[H(WD_p/2 - \pi D_p^2/8)]$. When $De'_{adv} \gtrsim 1$, chains are not elongated as they enter the next pore body, thereby promoting the eddy-free state in the current pore and the downstream pore as well. For our experiments in the unstable regime, De'_{adv} ranges from ≈ 0.7 to 5 using $\lambda_{ret} \sim \lambda \approx 1$ s, although these values again likely underestimate De'_{adv}. Thus, similar to the eddy-dominated state, we expect the eddy-free state to persist in the pore body over time before random flow fluctuations cause it to switch to the eddy-dominated state, consistent with our measurements shown in figure 7(*g–i*). Moreover, we again expect the eddy-free state to be correlated between neighbouring pores.

3.3.2. *Temporal and spatial characteristics of the flow*

The hypothesis presented in § 3.3.1 makes two testable predictions: first, that the two different unstable flow states each persist over long times before randomly switching, and second, that the flow states between neighbouring pores n and $n + 1$ are correlated. We test these predictions by investigating the temporal and spatial characteristics of the pore-scale flow. Specifically, we simultaneously image two neighbouring pores within the medium, pores $n = 21$ and $n + 1 = 22$, at $M = 15$ and monitor the flow states for $2500\tau_{pv}$. Figure 8(*a*) shows a snapshot of the flow pathlines imaged simultaneously and averaged over $10\tau_{pv}$ at an instance when both pores are in the eddy-dominated state.

The data in figure 7(*g–i*) support the first prediction that the two distinct flow states persist over long times. To further test this prediction, we measure the distribution of durations over which each flow state persists in a given pore before switching to the other state; we define a switching event as the instant when the total eddy area A_{total} in a given pore crosses a threshold value of $0.05\ A_{pore}$. This threshold is motivated by the clear separation between the eddy-dominated and eddy-free states indicated by the probability density function in figure 4(*c*). In agreement with our expectation, we find a broad distribution of long flow persistence times with no characteristic persistence time, as shown by the navy blue points in figure 8(*b*) – confirming our first prediction. Indeed, theoretical predictions for two-state systems that have self-stabilizing states – similar to the eddy-dominated and eddy-free states described here – also predict broad distributions of state persistence times (Ali, Wingreen & Mukhopadhyay 2018).

The image in figure 8(*a*) supports the second prediction that the flow states in neighbouring pores are correlated. To further test this prediction, we measure the instantaneous total eddy areas $A_{total,n}$ and $A_{total,n+1}$ in pores $n = 21$ and $n + 1 = 22$ by imaging both pores simultaneously over several thousand τ_{pv}. To visualize the pathlines of the individual tracer particles, we average successive frames for $10\tau_{pv}$; this procedure enables us to determine the presence or absence of recirculating eddies in the pore bodies and provides a way to directly measure the eddy areas by tracking the eddy boundaries, as exemplified in figure 8(*a*). We thereby compute the total eddy area A_{total} in each pore body of area A_{pore}. Over the course of this experiment, the pore bodies exhibit the full range of flow behaviours: we measure the full range of possible total eddy sizes for each pore body, ranging from $A_{total} = 0$ to the maximal value $A_{total} \approx 0.5A_{pore}$. Then, to quantify the correlation in flow state between pores n and $n+1$, we plot the total eddy areas simultaneously measured for both pores at different times, $A_{total,n}$ and $A_{total,n+1}$, respectively. These measurements show a positive correlation between the instantaneous flow states of neighbouring pores $n = 21$ and $n + 1 = 22$ over the imaging duration, as shown by the navy

https://doi.org/10.1017/jfm.2020.122 Published online by Cambridge University Press

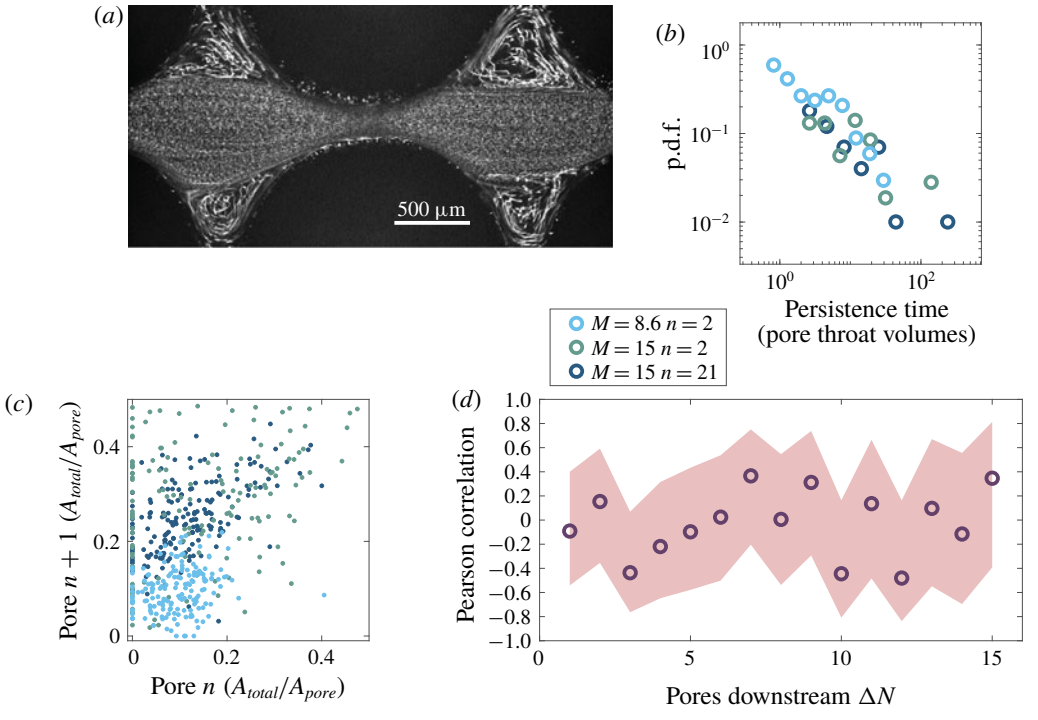


FIGURE 8. (*a*) Simultaneous pathline imaging of pores 21 and 22 averaged over $10\tau_{pv}$ for $M = 15.0$. Both pores are in the eddy-dominated state. (*b*) Probability density function of times between discrete switching events, representing the duration over which a given flow state persists in pores n or $n + 1$, for pores imaged over at least $400\tau_{pv}$. For panels (*b*) and (*c*), light blue shows $M = 8.6$ for $n = 2$, teal blue shows $M = 15$ for $n = 2$, and navy blue shows $M = 15$ for $n = 21$. The data are broadly distributed with long tails. (*c*) Instantaneous eddy areas of pores n and pore $n + 1$ are positively correlated, indicating that flow states are correlated between neighbouring pores. (*d*) Pearson correlation coefficients between pores separated by a length $l_s\Delta N$ and imaged sequentially a time $80\tau_{pv}\Delta N$ apart for $M = 15.0$. The flow state of each pore is averaged over $80\tau_{pv}$. Thus, this analysis only quantifies any possible long-time correlations that persist over time scales larger than $80\tau_{pv}\Delta N$. Light red shaded region indicates 99 % confidence interval for estimated correlation coefficient given the sampling size.

blue points in figure 8(*c*). We quantify this correlation using the Pearson correlation coefficient $\rho_{n,n+1} \equiv \mathrm{cov}(A_{total,n},\ A_{total,n+1})/[\sigma(A_{total,n})\sigma(A_{total,n+1})]$, where cov is the covariance and σ is the standard deviation of the instantaneous measurements of $A_{total,n}$ and $A_{total,n+1}$ over the different times. We find $\rho_{21,22} = 0.55 > 0$, confirming a positive correlation between the eddy sizes in the neighbouring pores 21 and 22 that is statistically significant ($p < 0.001$, two-tailed t-test). Thus, the unstable flow states in neighbouring pores are correlated with each other, confirming our second prediction.

To further test how this behaviour varies spatially and with M, we repeat these measurements near the inlet at pores $n = 2$ and $n + 1 = 3$ at two different flow rates corresponding to $M = 15$ and $M = 8.6$. We expect that decreasing the flow rate will

https://doi.org/10.1017/jfm.2020.122 Published online by Cambridge University Press

decrease the advective Deborah numbers De_{adv} and De'_{adv}; thus we expect that at lower flow rates, unstable flow states will still be broadly distributed, but will persist over shorter time scales. Our data confirm this expectation: we find that at the lower flow rate, flow states persist for slightly shorter times, as indicated by the light blue points ($M = 8.6$, $n = 2$) compared to the teal blue points ($M = 15$, $n = 2$) shown in figure 8(*b*). The unstable flow states in neighbouring pores remain positively correlated with each other in both cases, as shown by the light blue and teal blue points in figure 8(*c*); the corresponding Pearson correlation coefficients are $\rho_{2,3} = 0.25 > 0$ and $\rho_{2,3} = 0.21 > 0$, respectively, confirming a positive correlation that is statistically significant ($p < 0.001$, two-tailed t-test). This positive correlation likely reflects the fact that, even at the lower flow rate with $M = 8.6$, both $De_{adv} \approx 0.5$ and $De'_{adv} \approx 0.7$ are close to one, and thus, flow states are still likely to be correlated between neighbours. Intriguingly, while the correlation coefficient does not depend strongly on M for this range of flow rates, it does increase with position along the flow direction: for the same $M = 15$, $\rho_{2,3} = 0.21$ while $\rho_{21,22} = 0.55$, suggesting that flow states in neighbouring pores become increasingly correlated downstream. Further exploring this spatial dependence of correlations in unstable flow state will be a useful direction for future work.

While neighbouring pores exhibit correlated flow states on short time scales, imaging of flow through the entire medium (figure 6) suggests that these correlations are not sufficient to produce long-range correlations in the flow over long times. Indeed, as quantified by the measurements in figure 8(*b*), we do not expect correlations to persist, even for neighbouring pores, when flow state is averaged over sufficiently long time scales. To test this expectation, we sequentially image pores $n = 2$ through $n = 30$ for $80\tau_{pv}$ each. We use these data to compute the time-averaged eddy area in each pore, $\bar{A}_{total,2}$ through $\bar{A}_{total,30}$, where each value of $\bar{A}_{total}$ is averaged over $80\tau_{pv}$. We then quantify any possible correlations between these 29 measurements of the time-averaged eddy areas using the correlation coefficient $\rho_{n,n+\Delta N} \equiv \mathrm{cov}(\bar{A}_{total,n}, \bar{A}_{total,n+\Delta N})/[\sigma(\bar{A}_{total,n})\sigma(\bar{A}_{total,n+\Delta N})]$, which in this case quantifies correlations between the measured $\bar{A}_{total}$ for all pores n and $n + \Delta N$ that are thus separated by a length $l_s\Delta N$; here, cov is the covariance and σ is the standard deviation of the time-averaged measurements of $\bar{A}_{total,n}$ and $\bar{A}_{total,n+\Delta N}$, for a given value of ΔN ranging from 1 to 15, over the different values of n. In this analysis, instead of tracking the instantaneous correlation for many different time points as before, we track a time-averaged correlation for many different pairs of pores. Thus, this correlation analysis does not capture any possible flow correlations ΔN pores apart those that arise on time scales shorter than $80\tau_{pv}\Delta N$: it only quantifies any possible long-time correlations that persist over time scales larger than $80\tau_{pv}\Delta N$. Consistent with our expectation, we do not find long-time correlations in flow state, even between nearest neighbours: the correlation coefficient does not statistically deviate from zero for any values of ΔN throughout the medium, as shown in figure 8(*d*). Thus, while unstable flow states are correlated over short times across neighbouring pores, these correlations do not persist over long time scales – presumably due to the influence of random fluctuations in the flow, which likely promote switching between flow states. Our data do not preclude the possibility that longer-range correlations may arise at shorter time scales, or that correlations in flow state can evolve spatially throughout the medium; indeed, previous work has indicated that velocity correlations can coherently propagate through other experimental geometries (Qin *et al.* 2019). Investigating whether the flow correlations described in figure 8(*a–c*) can persist over broader spatial and temporal ranges will be a useful direction for future work.

https://doi.org/10.1017/jfm.2020.122 Published online by Cambridge University Press

4. Conclusions

Our work describes the first experimental observations of bistability in the flow of an elastic polymer solution through porous media, confirming previous theoretical predictions (Avgousti & Beris 1993; Sureshkumar *et al.* 1994; Varshney & Steinberg 2017). We find that when the spacing between pores is sufficiently small, and when the imposed flow rate is sufficiently large, the flow stochastically switches between two distinct unstable flow states. In the eddy-dominated state, a pair of large unstable eddies forms in the corners of a pore body, while in the eddy-free state, strongly fluctuating fluid pathlines fill the entire pore body and eddies do not form. Our results thus indicate that in a porous medium the pore-scale flow behaviour may not be determined just by injection conditions – as quantified by the Weissenberg number *Wi* or the *M* parameter (McKinley *et al.* 1996; Pakdel & McKinley 1996) – and the geometry of the individual pores, as is often assumed.

Our model 1-D geometry does not incorporate pore size disorder, tortuosity and connectivity for simplicity; it instead provides a way to isolate and systematically probe the role of pore spacing on flow behaviour. Incorporating these additional complexities in the medium geometry, and extending our findings to 2-D and 3-D media in which transverse interactions between pores may also play a role (Talwar & Khomami 1995; Khomami & Moreno 1997; Arora *et al.* 2002; Sadanandan & Sureshkumar 2004; Vázquez-Quesada & Ellero 2012; Howe, Clarke & Giernalczyk 2015; Clarke *et al.* 2016; De *et al.* 2017*a*,*b*,*c*,*d*, 2018*a*,*b*; Kawale *et al.* 2017*b*,*a*; Walkama, Waisbord & Guasto 2019), will be an important direction for future studies. Moreover, because pressure drop measurements are often used to characterize flow through porous media (Sandiford *et al.* 1964; Chauveteau & Moan 1981; Durst *et al.* 1981; Chauveteau *et al.* 1984; Pitts *et al.* 1995; Wang *et al.* 2011*a*; Vermolen *et al.* 2014; Wei *et al.* 2014), exploring the connection between unstable flow states and the macroscopic pressure drop across the medium will also be an important extension of our work.

We hypothesize that the flow bistability arises from the interplay between flow-induced polymer elongation, which promotes eddy formation, and relaxation of polymers as they are advected between pores, which enables the eddy-free state to form. Consistent with this idea, we find that the eddy sizes increase with the imposed flow rate. Additionally, we find that a flow state in a given pore persists over long time scales before switching to the other flow state, presumably due to random flow fluctuations. Flow state is also strongly correlated between neighbouring pores at short time scales; however, these correlations are not sufficient to produce correlations in the flow through the entire medium over long times. Elucidating the factors that determine the length and time scales over which flow correlations persist will be an interesting direction for future work.

While our experiments probe the case of dilute polymer solutions – in which polymer overlap likely does not influence flow behaviour – flow behaviour is known to change considerably at higher concentrations due to the increased propensity of polymer chains to overlap (Kawale *et al.* 2017*a*,*b*). We therefore expect that in more concentrated solutions, overlap of polymer chains will increase the relaxation and retardation times λ_{rel} and λ_{ret}, leading to larger values of the advective Deborah numbers De_{adv} and De'_{adv}. Thus, we expect that more concentrated polymer solutions will have correlated flow states that span more pores and that persist over longer time scales.

https://doi.org/10.1017/jfm.2020.122 Published online by Cambridge University Press

The different spatial and temporal characteristics of the two flow states described here could impact fluid mixing and the displacement of trapped immiscible fluids from the pore space in a variety of ways (Babayekhorasani *et al.* 2016; Aramideh, Vlachos & Ardekani 2019). Thus, a deeper understanding of these flow behaviours could provide guidance to applications that require specific mixing or fluid displacement behaviours. Examples include oil recovery and groundwater remediation, in which the viscous forces exerted by the polymer solution could displace a trapped fluid from the pores, or unstable mixing due to the fluid instability could improve the transport of oxidants and surfactants to the fluid interface. Such flow behaviours could also be harnessed in other emerging applications such as controlling mixing and flow in lab-on-a-chip devices, filtration and extrusion of polymeric resins during 3-D printing.

Acknowledgements

It is a pleasure to acknowledge G. H. McKinley, P. D. Olmsted, A. Z. Panagiotopoulos, R. K. Prud'homme, B. Qin and H. A. Stone for stimulating discussions, and the Stone Lab for access to the SLA printer and the rheometer. Acknowledgement is made to the Donors of the American Chemical Society Petroleum Research Fund for partial support of this research (PRF# no. 59026-DNI9). This material is also based upon work supported by the National Science Foundation Graduate Research Fellowship Program (to C.A.B.) under grant no. DGE-1656466. Any opinions, findings and conclusions or recommendations expressed in this material are those of the authors and do not necessarily reflect the views of the National Science Foundation. C.A.B. was also supported in part by the Mary and Randall Hack Graduate Award of the Princeton Environmental Institute. A.S. was supported in part by the Lidow Thesis Fund at Princeton University and the Dede T. Bartlett P03 Fund for Student Research through the Andlinger Center for Energy and the Environment.

Declaration of interests

The authors report no conflict of interest.

Appendix

The channel dimensions and polymer concentration used in our experiments enable us to isolate the influence of polymer elongation and relaxation between pores, with a minimal influence of polymer surface adsorption, flow-induced chain migration, wall slip, and shear banding, as quantitatively assessed below.

The first effect – polymer adsorption to the solid surfaces and eventual blockage of pore throats – has been documented for media with small pores (Zaitoun *et al.* 1988; Zitha, Chauveteau & Zaitoun 1995; Zaitoun *et al.* 1998; Obey & Griffiths 1999; Zitha, Chauveteau & Léger 2001). However, this effect typically influences flow behaviour in media having pore throats much smaller than those explored in our work: the steady state thickness of adsorbed polymers is of the order of polymer molecular dimensions, and for the HPAM polymer used in our experiments, this thickness is $\sim$100 nm (Grattoni *et al.* 2004). Since the thickness of this adsorbed layer is over three orders of magnitude smaller than the smallest channel dimension $L_c = 400$ μm in our experiments, we do not expect this adsorption layer to appreciably impact the flow. Furthermore, pore blockage is typically exacerbated by the bridging of elongated polymers across the pore throats (Zitha *et al.* 2001); however, the fully elongated

https://doi.org/10.1017/jfm.2020.122 Published online by Cambridge University Press

contour length of the HPAM polymer is $NL_{mon} \approx 40$ μm, where N is the degree of polymerization and L_{mon} is the monomer Kuhn length. Since this fully elongated contour length is an order of magnitude smaller than the smallest channel dimension L_c, we again do not expect polymer blockage of the pore throats to play a considerable role in our experiments.

Similarly, while flow-induced chain migration and wall slip frequently arise in confined flows of polymer solutions, they give rise to polymer concentration inhomogeneities over length scales ∼0.1 to 10 μm (Kekre, Butler & Ladd 2010), one to three orders of magnitude smaller than L_c. We estimate this length scale by balancing the influence of chain diffusion with elastic normal stresses (Ma & Graham 2005): $L_d = (9\sqrt{\pi}/128)((N_1 - N_2)/nk_BT)h^*R_g$, where n is the polymer number density in the bulk solution, k_BT is thermal energy, and R_g is the polymer radius of gyration. To determine an upper bound for L_d, we take the value of the first normal stress difference N_1 at the maximal shear rate using our shear rheology measurements, and take the second normal stress difference N_2 to be zero. The parameter $h^* = (\zeta/\eta_s)\sqrt{H/36\pi^3 k_BT} = 0.07$ quantifies hydrodynamic interactions, where η_s is the shear viscosity of the background solvent, $H \approx k_BT/2R_g^2$ is a characteristic polymer spring constant, $\zeta \approx 4H\lambda$ is the monomer hydrodynamic friction coefficient and λ is the polymer relaxation time estimated using shear rheology as described in § 2. Using these values, we obtain $L_d \approx 20R_g = 4$ μm – in reasonable agreement with measurements that indicate $L_d \approx NL_{mon}/3 \approx 14$ μm (Fang, Hu & Larson 2005). These estimated values are one to two orders of magnitude smaller than L_c; thus, we do not expect flow-induced migration to appreciably impact the flow.

Polymer wall slip can play a key role when the flow channel has dimensions approaching molecular dimensions, and for concentrated polymer solutions with a high viscosity ratio $\beta \equiv \eta_0/\eta_s$, where η_0 is the maximal solution shear viscosity and η_s is the shear viscosity of the background solvent. However, in our experiments, L_c is three orders of magnitude larger than R_g, and our polymer solution is dilute, with $\beta = 1.7$ close to one. Indeed, an upper bound for the length scale over which wall slip occurs L_s can be estimated (Wang, Ravindranath & Boukany 2011*b*) as $L_s \leqslant \beta R_g = 330$ nm. This value is over three orders of magnitude smaller than L_c; thus, we do not expect that wall slip appreciably impacts the flow. Further, we can use this length scale to estimate an upper bound for the wall slip speed U_s using the wall shear rate $\dot{\gamma}$ in the pore throat at the highest flow rate tested in our experiments; we calculate $U_s \leqslant L_s\dot{\gamma} \approx 7$ μm s⁻1, over two orders of magnitude smaller than the characteristic flow speeds explored in our experiments. This estimate again suggests that wall slip does not appreciably impact the flow.

Shear banding of polymers often arises during the flow of concentrated polymer solutions. However, our experiments probe the case of dilute polymer solutions, in which polymer overlap likely does not influence flow behaviour and in which shear banding is not expected to occur (Wang *et al.* 2011*b*). This expectation is further supported by our shear rheology measurements: over the experimental range of shear rates, our measurements of rate-controlled shear rheology indicate that the shear stress varies approximately linearly with shear rate, with a shear thinning exponent ≈ 0.92; by contrast, shear banding typically occurs for solutions in which the shear stress varies non-monotonically with imposed shear rate (Fielding 2007; Olmsted 2008). We therefore do not expect that shear banding plays an appreciable role in our experiments.

https://doi.org/10.1017/jfm.2020.122 Published online by Cambridge University Press

REFERENCES

ALI, M. Z., WINGREEN, N. S. & MUKHOPADHYAY, R. 2018 Hidden long evolutionary memory in a model biochemical network. *Phys. Rev.* E **97** (4), 040401.

ARAMIDEH, S., VLACHOS, P. P. & ARDEKANI, A. M. 2019 Nanoparticle dispersion in porous media in viscoelastic polymer solutions. *J. Non-Newtonian Fluid Mech.* **268**, 75–80.

ARORA, K., SURESHKUMAR, R. & KHOMAMI, B. 2002 Experimental investigation of purely elastic instabilities in periodic flows. *J. Non-Newtonian Fluid Mech.* **108** (1-3), 209–226.

AVGOUSTI, M. & BERIS, A. N. 1993 Non-axisymmetric modes in viscoelastic Taylor–Couette flow. *J. Non-Newtonian Fluid Mech.* **50** (2-3), 225–251.

BABAYEKHORASANI, F., DUNSTAN, D. E., KRISHNAMOORTI, R. & CONRAD, J. C. 2016 Nanoparticle dispersion in disordered porous media with and without polymer additives. *Soft Matt.* **12** (26), 5676–5683.

BALKOVSKY, E., FOUXON, A. & LEBEDEV, V. 2000 Turbulent dynamics of polymer solutions. *Phys. Rev. Lett.* **84** (20), 4765–4768.

BATCHELOR, G. K. 1971 The stress generated in a non-dilute suspension of elongated particles by pure straining motion. *J Fluid Mech.* **46** (4), 813–829.

BERNABE, Y. 1991 Pore geometry and pressure dependence of the transport properties in sandstones. *Geophysics* **56** (4), 424–576.

BLUNT, M. J. 2017 *Multiphase Flow in Permeable Media: A Pore-Scale Perspective*. Cambridge University Press.

BOGER, D. V. 1987 Viscoelastic flows through contractions. *Annu. Rev. Fluid Mech.* **19** (1), 157–182.

BROWNE, C. A., SHIH, A. & DATTA, S. S. 2019 Pore-scale flow characterization of polymer solutions in microfluidic porous media. *Small* **2019**, 1903944.

CHAUVETEAU, G. & MOAN, M. 1981 The onset of dilatant behaviour in non-inertial flow of dilute polymer solutions through channels with varying cross-sections. *J. Phys. Lett.* **42** (10), 201–204.

CHAUVETEAU, G., MOAN, M. & MAGUEUR, A. 1984 Thickening behaviour of dilute polymer solutions in non-inertial elongational flows. *J. Non-Newtonian Fluid Mech.* **16** (3), 315–327.

CHERTKOV, M. 2000 Polymer stretching by turbulence. *Phys. Rev. Lett.* **84** (20), 4761.

CLARKE, A., HOWE, A. M., MITCHELL, J., STANILAND, J. & HAWKES, L. A. 2016 How viscoelastic-polymer flooding enhances displacement efficiency. *SPE J.* **21** (03), 675–687.

CLASEN, C., PLOG, J. P., KULICKE, W.-M., OWENS, M., MACOSKO, C., SCRIVEN, L. E., VERANI, M. & MCKINLEY, G. H. 2006 How dilute are dilute solutions in extensional flows? *J. Rheol.* **50**, 849–881.

DATTA, S. S., CHIANG, H., RAMAKRISHNAN, T. S. & WEITZ, D. A. 2013 Spatial fluctuations of fluid velocities in flow through a three-dimensional porous medium. *Phys. Rev. Lett.* **111** (6), 064501.

DATTA, S. S., DUPIN, J.-B. & WEITZ, D. A. 2014*a* Fluid breakup during simultaneous two-phase flow through a three-dimensional porous medium. *Phys. Fluids* **26** (6), 062004.

DATTA, S. S., RAMAKRISHNAN, T. S. & WEITZ, D. A. 2014*b* Mobilization of a trapped non-wetting fluid from a three-dimensional porous medium. *Phys. Fluids* **26** (2), 022002.

DE, S., KOESEN, S. P., MAITRI, R. V., GOLOMBOK, M., PADDING, J. T. & VAN SANTVOORT, J. F. M. 2018*a* Flow of viscoelastic surfactants through porous media. *AIChE J.* **64** (2), 773–781.

DE, S., KRISHNAN, P., VAN DER SCHAAF, J., KUIPERS, J. A. M., PETERS, E. A. J. F. & PADDING, J. T. 2018*b* Viscoelastic effects on residual oil distribution in flows through pillared microchannels. *J. Colloid Interface Sci.* **510**, 262–271.

DE, S., KUIPERS, J. A. M., PETERS, E. A. J. F. & PADDING, J. T. 2017*a* Viscoelastic flow simulations in model porous media. *Phys. Rev. Fluids* **2** (5), 053303.

DE, S., KUIPERS, J. A. M., PETERS, E. A. J. F. & PADDING, J. T. 2017*b* Viscoelastic flow simulations in random porous media. *J. Non-Newtonian Fluid Mech.* **248**, 50–61.

DE, S., KUIPERS, J. A. M., PETERS, E. A. J. F. & PADDING, J. T. 2017*c* Viscoelastic flow past mono-and bidisperse random arrays of cylinders: flow resistance, topology and normal stress distribution. *Soft Matt.* **13** (48), 9138–9146.

DE, S., VAN DER SCHAAF, J., DEEN, N. G., KUIPERS, J. A. M., PETERS, E. A. J. F. & PADDING, J. T. 2017*d* Lane change in flows through pillared micro channels. *Phys. Fluids* **29**, 113102.

https://doi.org/10.1017/jfm.2020.122 Published online by Cambridge University Press

DOYEN, P. M. 1988 Permeability, conductivity, and pore geometry of sandstone. *J. Geophys. Res.* **93** (B7), 7729–7740.

DURST, F. R. B. U., HAAS, R. & KACZMAR, B. U. 1981 Flows of dilute hydrolyzed polyacrylamide solutions in porous media under various solvent conditions. *J. Appl. Polym. Sci.* **26** (9), 3125–3149.

FANG, L., HU, H. & LARSON, R. G. 2005 DNA configurations and concentration in shearing flow near a glass surface in a microchannel. *J. Rheol.* **49** (1), 127–138.

FIELDING, S. M. 2007 Complex dynamics of shear banded flows. *Soft Matt.* **3** (10), 1262–1279.

FRANÇOIS, N., AMAROUCHENE, Y., LOUNIS, B. & KELLAY, H. 2009 Polymer conformations and hysteretic stresses in nonstationary flows of polymer solutions. *Europhys. Lett.* **86** (3), 34002.

GALINDO-ROSALES, F. J., CAMPO-DEAÑO, L., PINHO, F. T., VAN BOKHORST, E., HAMERSMA, P. J., OLIVEIRA, M. S. N. & ALVES, M. A. 2012 Microfluidic systems for the analysis of viscoelastic fluid flow phenomena in porous media. *Microfluid. Nanofluid.* **12** (1-4), 485–498.

GALINDO-ROSALES, F. J., CAMPO-DEAÑO, L., SOUSA, P. C., RIBEIRO, V. M., OLIVEIRA, M. S. N., ALVES, M. A. & PINHO, F. T. 2014 Viscoelastic instabilities in micro-scale flows. *Exp. Therm. Fluid Sci.* **59**, 128–139.

GERASHCHENKO, S., CHEVALLARD, C. & STEINBERG, V. 2005 Single-polymer dynamics: coil-stretch transition in a random flow. *Europhys. Lett.* **71** (2), 221.

GRATTONI, C. A., LUCKHAM, P. F., JING, X. D., NORMAN, L. & ZIMMERMAN, R. W. 2004 Polymers as relative permeability modifiers: adsorption and the dynamic formation of thick polyacrylamide layers. *J. Petrol. Sci. Engng* **45** (3-4), 233–245.

GRILLI, M., VÁZQUEZ-QUESADA, A. & ELLERO, M. 2013 Transition to turbulence and mixing in a viscoelastic fluid flowing inside a channel with a periodic array of cylindrical obstacles. *Phys. Rev. Lett.* **110** (17), 174501.

GROISMAN, A. & STEINBERG, V. 2000 Elastic turbulence in a polymer solution flow. *Nature* **405** (6782), 53.

GULATI, S., MULLER, S. J. & LIEPMANN, D. 2015 Flow of DNA solutions in a microfluidic gradual contraction. *Biomicrofluidics* **9** (5), 054102.

GUPTA, V. K., SURESHKUMAR, R. & KHOMAMI, B. 2004 Polymer chain dynamics in Newtonian and viscoelastic turbulent channel flows. *Phys. Fluids* **16** (5), 1546–1566.

HARNETT, J. P. & IRVINE, T. F. 1979 *Advances in Heat Transfer*. Elsevier Science.

HAWARD, S. J., MCKINLEY, G. H. & SHEN, A. Q. 2016 Elastic instabilities in planar elongational flow of monodisperse polymer solutions. *Sci. Rep.* **6**, 33029.

HAWARD, S. J. & ODELL, J. A. 2003 Viscosity enhancement in non-Newtonian flow of dilute polymer solutions through crystallographic porous media. *Rheol. Acta* **42** (6), 516–526.

HAWARD, S. J., TODA-PETERS, K. & SHEN, A. Q. 2018 Steady viscoelastic flow around high-aspect-ratio, low-blockage-ratio microfluidic cylinders. *J. Non-Newtonian Fluid Mech.* **254**, 23–35.

HOWE, A. M., CLARKE, A. & GIERNALCZYK, D. 2015 Flow of concentrated viscoelastic polymer solutions in porous media: effect of MW and concentration on elastic turbulence onset in various geometries. *Soft Matt.* **11** (32), 6419–6431.

HUH, C., POPE, G. A. *et al.* 2008 Residual oil saturation from polymer floods: laboratory measurements and theoretical interpretation. In *SPE Symposium on Improved Oil Recovery*. Society of Petroleum Engineers.

IOANNIDIS, M. A. & CHATZIS, I. 1993 Network modelling of pore structure and transport properties of porous media. *Chem. Engng Sci.* **48** (5), 951–972.

KANG, P. K., DE ANNA, P., NUNES, J. P., BIJELJIC, B., BLUNT, M. J. & JUANES, R. 2014 Pore-scale intermittent velocity structure underpinning anomalous transport through 3D porous media. *Geophys. Res. Lett.* **41** (17), 6184–6190.

KAWALE, D., BOUWMAN, G., SACHDEV, S., ZITHA, P. L. J., KREUTZER, M. T., ROSSEN, W. R. & BOUKANY, P. E. 2017*a* Polymer conformation during flow in porous media. *Soft Matt.* **13** (46), 8745–8755.

https://doi.org/10.1017/jfm.2020.122 Published online by Cambridge University Press

KAWALE, D., MARQUES, E., ZITHA, P. L. J., KREUTZER, M. T., ROSSEN, W. R. & BOUKANY, P. E. 2017*b* Elastic instabilities during the flow of hydrolyzed polyacrylamide solution in porous media: effect of pore-shape and salt. *Soft Matt.* **13** (4), 765–775.

KEKRE, R., BUTLER, J. E. & LADD, A. J. C. 2010 Comparison of lattice-Boltzmann and Brownian-dynamics simulations of polymer migration in confined flows. *Phys. Rev.* E **82** (1), 011802.

KENNEY, S., POPER, K., CHAPAGAIN, G. & CHRISTOPHER, G. F. 2013 Large Deborah number flows around confined microfluidic cylinders. *Rheol. Acta* **52** (5), 485–497.

KHOMAMI, B. & MORENO, L. D. 1997 Stability of viscoelastic flow around periodic arrays of cylinders. *Rheol. Acta* **36** (4), 367–383.

KOELLING, K. W. & PRUD'HOMME, R. K. 1991 Instabilities in multi-hole converging flow of viscoelastic fluids. *Rheol. Acta* **30** (6), 511–522.

KWIECIEN, M. J., MACDONALD, I. F. & DULLIEN, F. A. L. 1990 Three dimensional reconstruction of porous media from serial section data. *J. Microsc.* **159** (3), 343–359.

LANZARO, A., CORBETT, D. & YUAN, X.-F. 2017 Non-linear dynamics of semi-dilute PAAm solutions in a microfluidic 3D cross-slot flow geometry. *J. Non-Newtonian Fluid Mech.* **242**, 57–65.

LANZARO, A., LI, Z. & YUAN, X.-F. 2015 Quantitative characterization of high molecular weight polymer solutions in microfluidic hyperbolic contraction flow. *Microfluid. Nanofluid.* **18** (5-6), 819–828.

LANZARO, A. & YUAN, X.-F. 2011 Effects of contraction ratio on non-linear dynamics of semi-dilute, highly polydisperse PAAm solutions in microfluidics. *J. Non-Newtonian Fluid Mech.* **166** (17-18), 1064–1075.

LARSON, R. G. 1992 Flow-induced mixing, demixing, and phase transitions in polymeric fluids. *Rheol. Acta* **31** (6), 497–520.

MA, H. & GRAHAM, M. D. 2005 Theory of shear-induced migration in dilute polymer solutions near solid boundaries. *Phys. Fluids* **17** (8), 083103.

MCKINLEY, G. H., PAKDEL, P. & ÖZTEKIN, A. 1996 Rheological and geometric scaling of purely elastic flow instabilities. *J. Non-Newtonian Fluid Mech.* **67**, 19–47.

MITCHELL, J., LYONS, K., HOWE, A. M. & CLARKE, A. 2016 Viscoelastic polymer flows and elastic turbulence in three-dimensional porous structures. *Soft Matt.* **12** (2), 460–468.

MONGRUEL, A. & CLOITRE, M. 1995 Extensional flow of semidilute suspensions of rod-like particles through an orifice. *Phys. Fluids* **7** (11), 2546–2552.

MONGRUEL, A. & CLOITRE, M. 2003 Axisymmetric orifice flow for measuring the elongational viscosity of semi-rigid polymer solutions. *J. Non-Newtonian Fluid Mech.* **110** (1), 27–43.

OBEY, T. M. & GRIFFITHS, P. C. 1999 Polymer adsorption: fundamentals. In *Principles of Polymer Science and Technology in Cosmetic and Personal Care* (ed. E. D. Goddard & J. V. Gruber), pp. 51–72. Marcel Dekker.

O'CONNELL, M. G., LU, N. B., BROWNE, C. A. & DATTA, S. S. 2019 Cooperative size sorting of deformable particles in porous media. *Soft Matt.* **15**, 3620.

ODELL, J. A. & HAWARD, S. J. 2006 Viscosity enhancement in non-Newtonian flow of dilute aqueous polymer solutions through crystallographic and random porous media. *Rheol. Acta* **45** (6), 853–863.

OLMSTED, P. D. 2008 Perspectives on shear banding in complex fluids. *Rheol. Acta* **47** (3), 283–300.

PAK, T., BUTLER, I. B., GEIGER, S., VAN DIJKE, M. I. J. & SORBIE, K. S. 2015 Droplet fragmentation: 3D imaging of a previously unidentified pore-scale process during multiphase flow in porous media. *Proc. Natl Acad. Sci. USA* **112** (7), 1947–1952.

PAKDEL, P. & MCKINLEY, G. H. 1996 Elastic instability and curved streamlines. *Phys. Rev. Lett.* **77** (12), 2459.

PAN, L., MOROZOV, A., WAGNER, C. & ARRATIA, P. E. 2013 Nonlinear elastic instability in channel flows at low Reynolds numbers. *Phys. Rev. Lett.* **110** (17), 174502.

PEARSON, J. R. A. 1976 Instability in non-Newtonian flow. *Annu. Rev. Fluid Mech.* **8** (1), 163–181.

PILITSIS, S. & BERIS, A. N. 1989 Calculations of steady-state viscoelastic flow in an undulating tube. *J. Non-Newtonian Fluid Mech.* **31** (3), 231–287.

https://doi.org/10.1017/jfm.2020.122 Published online by Cambridge University Press

PILITSIS, S. & BERIS, A. N. 1991 Viscoelastic flow in an undulating tube. Part II. Effects of high elasticity, large amplitude of undulation and inertia. *J. Non-Newtonian Fluid Mech.* **39** (3), 375–405.

PITTS, M. J., CAMPBELL, T. A., SURKALO, H., WYATT, K. *et al.* 1995 Polymer flood of the Rapdan pool, Saskatchewan, Canada. *SPE Res. Engng* **10** (03), 183–186.

QIN, B. & ARRATIA, P. E. 2017 Characterizing elastic turbulence in channel flows at low Reynolds number. *Phys. Rev. Fluids* **2** (8), 083302.

QIN, B., SALIPANTE, P. F., HUDSON, S. D. & ARRATIA, P. E. 2019 Upstream vortex and elastic wave in the viscoelastic flow around a confined cylinder. *J Fluid Mech.* **864**, R2.

RIBEIRO, V. M., COELHO, P. M., PINHO, F. T. & ALVES, M. A. 2014 Viscoelastic fluid flow past a confined cylinder: three-dimensional effects and stability. *Chem. Engng Sci.* **111**, 364–380.

RODD, L. E., COOPER-WHITE, J. J., BOGER, D. V. & MCKINLEY, G. H. 2007 Role of the elasticity number in the entry flow of dilute polymer solutions in micro-fabricated contraction geometries. *J. Non-Newtonian Fluid Mech.* **143** (2-3), 170–191.

ROOTE, D. S. 1998 In situ flushing. *Technology Status Report*. Ground Water Remediation Technology Analysis Center; available at http://www.gwrtac.org.

RUBINSTEIN, M. & COLBY, R. H. 2003 *Polymer Physics*. Oxford University Press.

SADANANDAN, B. & SURESHKUMAR, R. 2004 Global linear stability analysis of viscoelastic flow through a periodic channel. *J. Non-Newtonian Fluid Mech.* **122** (1-3), 55–67.

SANDIFORD, B. B. *et al.* 1964 Laboratory and field studies of water floods using polymer solutions to increase oil recoveries. *J. Petrol. Tech.* **16** (08), 917–922.

SCHROEDER, C. M., BABCOCK, H. P., SHAQFEH, E. S. G. & CHU, S. 2003 Observation of polymer conformation hysteresis in extensional flow. *Science* **301** (5639), 1515–1519.

SHI, X. & CHRISTOPHER, G. F. 2016 Growth of viscoelastic instabilities around linear cylinder arrays. *Phys. Fluids* **28** (12), 124102.

SHI, X., KENNEY, S., CHAPAGAIN, G. & CHRISTOPHER, G. F. 2015 Mechanisms of onset for moderate mach number instabilities of viscoelastic flows around confined cylinders. *Rheol. Acta* **54** (9-10), 805–815.

SON, Y. 2007 Determination of shear viscosity and shear rate from pressure drop and flow rate relationship in a rectangular channel. *Polymer* **48** (2), 632–637.

SORBIE, K. S. 2013 *Polymer-Improved Oil Recovery*. Springer.

SOUSA, P. C., PINHO, F. T., OLIVEIRA, M. S. N. & ALVES, M. A. 2015 Purely elastic flow instabilities in microscale cross-slot devices. *Soft Matt.* **11** (45), 8856–8862.

SURESHKUMAR, R., BERIS, A. N. & AVGOUSTI, M. 1994 Non-axisymmetric subcritical bifurcations in viscoelastic Taylor–Couette flow. *Proc. R. Soc. Lond.* A **447** (1929), 135–153.

SURESHKUMAR, R., BERIS, A. N. & HANDLER, R. A. 1997 Direct numerical simulation of the turbulent channel flow of a polymer solution. *Phys. Fluids* **9** (3), 743–755.

TALWAR, K. K. & KHOMAMI, B. 1995 Flow of viscoelastic fluids past periodic square arrays of cylinders: inertial and shear thinning viscosity and elasticity effects. *J. Non-Newtonian Fluid Mech.* **57** (2-3), 177–202.

TERRAPON, V. E., DUBIEF, Y., MOIN, P., SHAQFEH, E. S. G. & LELE, S. K. 2004 Simulated polymer stretch in a turbulent flow using Brownian dynamics. *J. Fluid Mech.* **504**, 61–71.

VANAPALLI, S. A., CECCIO, S. L. & SOLOMON, M. J. 2006 Universal scaling for polymer chain scission in turbulence. *Proc. Natl Acad. Sci. USA* **103** (45), 16660–16665.

VARSHNEY, A. & STEINBERG, V. 2017 Elastic wake instabilities in a creeping flow between two obstacles. *Phys. Rev. Fluids* **2** (5), 051301.

VÁZQUEZ-QUESADA, A. & ELLERO, M. 2012 SPH simulations of a viscoelastic flow around a periodic array of cylinders confined in a channel. *J. Non-Newtonian Fluid Mech.* **167**, 1–8.

VERMOLEN, E. C. M., VAN HAASTERECHT, M. J. T., MASALMEH, S. K. *et al.* 2014 A systematic study of the polymer visco-elastic effect on residual oil saturation by core flooding. In *SPE EOR Conference at Oil and Gas West Asia*. Society of Petroleum Engineers.

WALKAMA, D. M., WAISBORD, N. & GUASTO, J. S. 2019 Disorder suppresses chaos in viscoelastic flows. arXiv:1906.11868.

https://doi.org/10.1017/jfm.2020.122 Published online by Cambridge University Press

WANG, D., WANG, G., XIA, H. *et al.* 2011*a* Large scale high visco-elastic fluid flooding in the field achieves high recoveries. In *SPE Enhanced Oil Recovery Conference*. Society of Petroleum Engineers.

WANG, S.-Q., RAVINDRANATH, S. & BOUKANY, P. E. 2011*b* Homogeneous shear, wall slip, and shear banding of entangled polymeric liquids in simple-shear rheometry: a roadmap of nonlinear rheology. *Macromolecules* **44** (2), 183–190.

WEI, B., ROMERO-ZERÓN, L. & RODRIGUE, D. 2014 Oil displacement mechanisms of viscoelastic polymers in enhanced oil recovery (EOR): a review. *J. Petrol. Explor. Prod. Technol.* **4** (2), 113–121.

ZAITOUN, A., BERTIN, H., LASSEUX, D. *et al.* 1998 Two-phase flow property modifications by polymer adsorption. In *SPE/DOE Improved Oil Recovery Symposium*. Society of Petroleum Engineers.

ZAITOUN, A, KOHLER, N *et al.* 1988 Two-phase flow through porous media: effect of an adsorbed polymer layer. In *SPE Annual Technical Conference and Exhibition*. Society of Petroleum Engineers.

ZAMI-PIERRE, F., DE LOUBENS, R., QUINTARD, M. & DAVIT, Y. 2016 Transition in the flow of power-law fluids through isotropic porous media. *Phys. Rev. Lett.* **117** (7), 074502.

ZILZ, J., POOLE, R. J., ALVES, M. A., BARTOLO, D., LEVACHÉ, B. & LINDNER, A. 2012 Geometric scaling of a purely elastic flow instability in serpentine channels. *J. Fluid Mech.* **712**, 203–218.

ZITHA, P., CHAUVETEAU, G., ZAITOUN, A. *et al.* 1995 Permeability dependent propagation of polyacrylamides under near-wellbore flow conditions. In *SPE International Symposium on Oilfield Chemistry*. Society of Petroleum Engineers.

ZITHA, P. L. J., CHAUVETEAU, G. & LÉGER, L. 2001 Unsteady-state flow of flexible polymers in porous media. *J. Colloid Interface Sci.* **234** (2), 269–283.

https://doi.org/10.1017/jfm.2020.122 Published online by Cambridge University Press